Are narrow spatial aftershock zones specific to fluid-induced earthquakes?

Kamran Karimi[1], **Jörn Davidsen**[1,2]

[1]Department of Physics and Astronomy, University of Calgary, 2500 University Drive NW, Calgary, Alberta, Canada T2N 1N4
[2]Hotchkiss Brain Institute, University of Calgary, 3330 Hospital Dr NW, Calgary, Alberta T2N 4N1, Canada

Key Points:

- Significant event-event triggering is present in both natural swarms and induced seismicity
- Narrow aftershock zones are not specific to induced seismicity but also occur in natural swarms
- Aftershock productivity might allow to distinguish between natural swarms and induced seismicity

Corresponding author: Kamran Karimi, kamran.karimi1@ucalgary.ca

Abstract

Aftershock cascades play an important role in forecasting seismicity in natural and human-made situations. While their behavior including the spatial aftershock zone has been the focus of many studies in tectonic settings, this is not the case when fluid flows are involved. Using high-quality seismic catalogs, we probe earthquake-earthquake triggering in three settings influenced by fluids: *i*) A natural swarm (Long Valley Caldera, California), *ii*) *suspected* swarms in the Yuha Desert (California), and *iii*) induced seismicity in Oklahoma and southern Kansas. All settings exhibit significant aftershock behavior highlighting the importance of secondary processes. The spatial aftershock zones scale with mainshock magnitude as expected based on the rupture length. While *i*) and *iii*) show a rapid decay beyond their rupture length, *ii*) exhibits long-range behavior suggesting that fluid migration might not be the dominant mechanism. We also find that aftershock productivity might allow to distinguish between natural swarms and induced seismicity.

Plain Language Summary

While it is known that fluid injection operations can induce seismic activity, it has remained unclear how this activity compares to their natural counterpart, seismic swarms driven by natural fluid flows. The latter are typically characterized by the absence of a dominant event within the seismic sequence, while exhibiting other characteristics consistent with tectonic aftershock sequences and secondary triggering. Our analysis of high-quality seismic catalogs for both types of fluid-induced seismicity shows that both exhibit a significant amount of secondary processes leading to *spatially localized* event-event triggering. Yet, the seismic productivity, which refers to the average increase in the number of aftershocks with the magnitude of their trigger, is significantly higher in the induced setting. Both findings are of direct importance for earthquake forecasting and seismic hazard assessment.

1 Introduction

Fluid-induced seismicity typically refers to (minor) seismic events that (partially) involve fluid flows. Examples range from *natural* flows associated with rainfalls and volcanic eruptions to *human-made* contexts including wastewater injection wells, hydraulic fracturing, and geothermal power plants. Recently, *anthropogenic* sources have lead to an extraordinary surge of seismic activities in different parts of the United States (Ellsworth, 2013). The most extreme cases are reported in Oklahoma and Southern Kansas where most seismic events are potentially linked to large-scale wastewater disposals. The USG survey indicates that no more than five (tectonic) earthquakes per year with magnitude $m \geq 3$ had been previously reported over almost three decades (Deflandre, 2016), in sharp contrast to the one thousand $m \geq 3$ earthquakes recorded in 2016. In this context, it is essential to identify potential anthropogenic origins and relevant secondary triggering mechanisms, which has important consequences in terms of seismic hazard assessment, earthquake forecasting and effective mitigation strategies.

To what extent fluid-based anthropogenic seismicity bears similarities with its natural analog is an open question. Swarm-like features of induced seismicity associated with wastewater disposal and/or hydraulic fracturing were found in (Skoumal et al., 2015). Signatures of event-event triggering or aftershock dynamics were recently reported in (Maghsoudi et al., 2016, 2018), where common features of event-event triggering and natural earthquake swarms, *i.e.* productivity relation or the Omori-Utsu (OU) relation as well as an absence of Båth's law, were recovered within the context of hydraulic fracturing-induced microseismicity. Recent studies point to pore-pressure fluctuations, poro-elastic effects, or combination of those two as relevant activation mechanisms (T. H. Goebel & Brodsky, 2018) as well as aseismic creep (Eyre et al., 2019). The signatures of event-event triggering in induced settings also indicate the relevance of static stress transfer, similar to the case of aftershocks

in tectonic settings (Maghsoudi et al., 2018). In general, the features of the spatio-temporal evolution of induced seismicty can be viewed as a main signature of the underlying physical activation and secondary triggering processes. For example, the typical diffusion-based picture is that the activation takes place in a spatially *local* manner and over diffusion timescales giving rise to a square-root time dependence of the distance (Shapiro, 2015). On the other hand, the overall increase in the spatial extent of induced seismicity could be interpreted in terms of poro-elastic interactions between migrating fluids and embedding porous solids (T. H. Goebel & Brodsky, 2018).

To which degree the mechanisms are affected by the specific source — anthropogenic or natural sources — has remained largely unexplored. Here, our aim is to identify commonalities and differences in the spatio-temporal dynamics of induced and natural seismicity in fluid-driven situations. To this end, we analyzed aftershocks properties in *i*) Oklahoma and southern Kansas and compared our observations with two other case studies, which are *ii*) the Long Valley Caldera and *iii*) the Yuha Desert, whose seismic activities are believed to be strongly influenced by the natural migration of fluids. Our overall methodology is similar to the one used by Vasylkivska and Huerta (2017); Schoenball and Ellsworth (2017a) in Oklahoma and Kansas aiming to distinguish between background events (as a direct consequence of fluid injection) and triggered events (due to secondary mechanisms).

All settings exhibit a significant amount of event-event triggering highlighting the importance of secondary processes for the overall seismicity. The event-event triggering rates in *i*) exhibit similar temporal features to those of natural earthquakes in *ii*), *iii*) and can be quantified by the OU relation (Kagan, 2013). In all cases, the productivity relation between the total number of aftershocks and the triggers' magnitude also holds, yet the number of triggered events increases much more rapidly with magnitude for *i*). The spatial clustering of aftershocks in *i*) is quantified by a steep algebraic decay with distance beyond the rupture length of the main shock. This agrees closely with the narrow aftershock zones associated with natural swarms in *ii*) suggesting that short-ranged triggering is not specific to human-made contexts. Moreover, we find analogous *topological* features associated with triggering cascades in *i*) and *ii*) confirming the swarm-like nature of induced seismicity in the former. In *iii*), however, aftershock sequences tend to be *burst-like* and the aftershock zones extend well beyond the associated rupture size. In fact, the fluid diffusion may not be the dominant contribution in *iii*) and other mechanisms — such as non-local stress transfer and aseismic deformations — and/or the underlying fault network might be more relevant in this context.

2 Data

We analyze three different, previously published high-resolution seismic catalogs, for which fluids are thought to play a significant role in driving seismic activity. For the injection-induced seismicity in Oklahoma and southern Kansas, we use a relocated catalog (Schoenball & Ellsworth, 2017a, 2017b). The region witnessed an almost ten fold increase in the overall seismicity rate over two years, which declined later on due to scaling down of industrial operations (Langenbruch & Zoback, 2016). A magnitude 5.8 earthquake occurred during this mitigation period and led to a spontaneous increase in the seismic activity indicating the significance of *secondary* triggering processes and aftershocks (Fig. S1(a) in SM). The Yuha Desert catalog (Ross et al., 2017) contains pronounced aftershock activity following the 2010 magnitude 7.2 El Mayor-Cucapah event (Fig. S1(b) in SM). We neglect the initial ten days after the event during which the seismic activity is mostly affected by aseismic deformations and instead, we focus on the later times, suggested to be driven by fluid diffusion (Ross et al., 2017). The Long Valley Caldera catalog (Shelly et al., 2016) corresponds to a five-month sequence of natural swarms (Fig. S1(c) in SM).

In all cases, the frequency-magnitude distributions largely follow the Gutenberg-Richter (GR) relation $N(\text{Mag.} > m) \propto 10^{-b(m-m_c)}$ (right panels of Fig. S1(a-c) in SM). Here, the

b-value controls the exponential decay rate and m_c denotes the magnitude of completeness. We vary m_{th} and include events with $m \geq m_{th}$ to estimate $b(m_{th})$ based on the maximum-likelihood estimator (Bhattacharya et al., 2011). We estimate both b and m_c by identifying the lowest value of m_{th} for which b becomes constant (Davidsen et al., 2015). For Oklahoma and southern Kansas (Fig. S1(a)), we obtain $b = 1.65$. The high b-value implies an excessive number of lower-magnitude earthquakes compared to tectonic settings, which typically exhibit $b \simeq 1$ (Kagan, 2013). Yet, similarly high b-values are observed for microseismic events associated with hydraulic fracturing (Eaton et al., 2014; Eaton & Maghsoudi, 2015; Maghsoudi et al., 2016; Dinske & Shapiro, 2013). For the Yuha Desert, we obtain $b = 0.95$ (Fig. S1(b)). The Long Valley catalog (Fig. S1(c)) is lacking a unique b-value. Our analysis indicates two regimes with $b = 0.7$ for $m_c = 0.2$ and $b = 0.9$ for $m_c = 1.0$. Thus, we use both sets of parameters for our triggering analysis. Using two different estimators (Kantz & Schreiber, 2004; Gneiting et al., 2012), the spatial distribution of hypocenters can be well approximated as a fractal with a fractal dimension $d_f \simeq 2$ for all catalogs.

3 Methodology: Event-event triggering and aftershock identification

We follow the methodology first proposed by (Zaliapin et al., 2008), which allows for a robust classification between triggered events (aftershocks) and events not triggered by other events in the catalog, considered background events (Zaliapin et al., 2008; Gu et al., 2013; Zaliapin & Ben-Zion, 2013; Moradpour et al., 2014; Davidsen et al., 2015; Schoenball et al., 2015; Davidsen & Baiesi, 2016; Davidsen et al., 2017; Maghsoudi et al., 2018; Teng & Baker, 2019). The starting point is the GR relation, which is used to formulate an expected magnitude-dependent rate of activity for a spatially uniform and stationary Poisson process. This rate allows one to formulate the null hypothesis of independent events — corresponding to background events — and the method seeks for possible rejections of it to identify triggered events and their trigger. As a first step, the present approach associates each event j to a set of possible triggers $\{i\}$ with $(t_i < t_j, \vec{r}_i, m_i)$ that fulfill $r_{ij} \equiv |\vec{r}_i - \vec{r}_j| \leq c_p\, t_{ij}$ with $t_{ij} \equiv t_j - t_i$ and pressure wave velocity $c_p \simeq 6$ km s^{-1} to ensure causality (Moradpour et al., 2014). The pair-wise quantity $n_{ij} \equiv c_g\, t_{ij}\, r_{ij}^{d_f}\, 10^{-b(m_i - m_c)}$ gives the expected number of magnitude m_i events between events i and j. Here, the prefactor c_g relates to the regional seismicity rate. We can set $c_g = 1$ without loss of generality. The most likely trigger i^* of event j can be identified by $n_j^* = \min_i\{n_{ij}\}$, since it is the strongest possible violation of the null hypothesis. Low values of n_j^* can be associated with triggered events and high values can be associated with background events. The separation between these groups can be readily seen in a two-dimensional projection of n_j^* using (t_j^*, r_j^*) defined as

$$\begin{aligned} t_j^* &\equiv t_{i^*j}\, 10^{-\frac{b}{2}(m_{i^*} - m_c)}, \\ r_j^* &\equiv r_{i^*j}^{d_f}\, 10^{-\frac{b}{2}(m_{i^*} - m_c)}, \end{aligned} \tag{1}$$

such that $n_j^* = r_j^* \times t_j^*$. Using the density distribution of n_j^* in this projection, one can choose a suitable threshold $n_{\rm th}$ for the separation (see SM for further discussion).

4 Results

Using the above methodology to identify event-event triggering, we find that all catalogs exhibit significant triggering and aftershocks (Fig. S2 in SM). This enables us to study the properties of the direct event-event triggering (the first generation of aftershocks) and their variations with time, distance, and magnitude.

4.1 Spatial aftershock zones

We evaluate the linear (normalized) aftershocks density $\rho_m(r)$ associated with triggers (or main shocks) of magnitude m. Displayed in the insets of Fig. 1(a-d), almost all aftershocks densities show an initial increase up to a peak followed by a power-law like decrease.

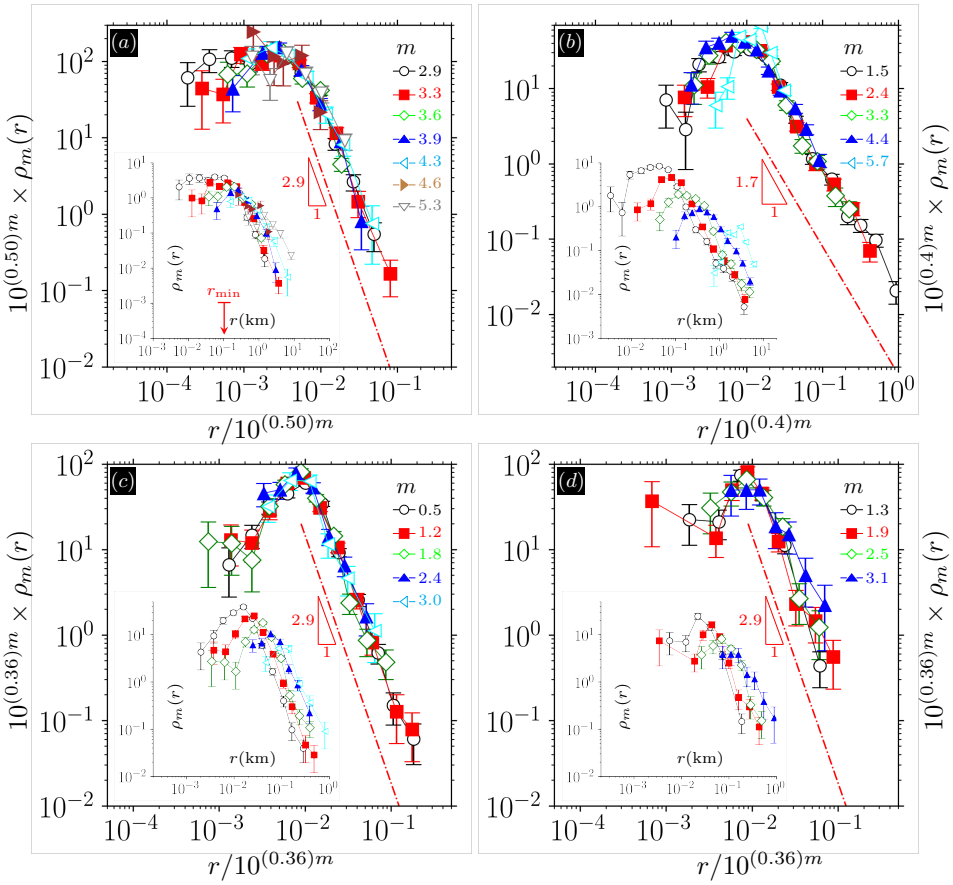

Figure 1. Rescaled probability density function of aftershocks $10^{\sigma m} \times \rho_m(r)$ against scaled distance $r/10^{\sigma m}$ in **a)** Oklahoma and southern Kansas **b)** the Yuha Desert **c)** Long Valley Caldera with $b = 0.7, m_c = 0.2$ **d)** Long Valley Caldera with $b = 0.9, m_c = 1.0$ conditioned based on the mean main shock magnitude m in a given range. The dash-dotted lines indicate $\rho(r) \propto r^{-\nu}$ for large r. The insets show the unrescaled data presented in the main plots. The red arrow indicates the average relative location uncertainty where available.

As for tectonic events (Gu et al., 2013), the location of the peak is closely aligned with the rupture length of the trigger, which scales as $r_{\text{rup}} \propto 10^{\sigma m}$. To test this explicitly, we rescale the distance r with $10^{\sigma m}$ and we indeed obtain a robust data collapse of all aftershock densities for a given catalog in Fig. 1(a-d). The variation between the different catalogs is minimal, namely $0.36 < \sigma < 0.5$, which is consistent with previously reported estimates for tectonic earthquakes (Leonard, 2010; Brengman et al., 2019; Moradpour et al., 2014). The data collapses also indicate that beyond the rupture length the aftershock density decays as $r^{-\nu}$. While aftershock zones in Oklahoma and southern Kansas as well as in the Long Valley Caldera exhibit a steep decay with $\nu \simeq 2.9$, the Yuha Desert data indicate a longer-ranged trend ($\nu \simeq 1.7$), typical of tectonic seismicity in southern California (Gu et al., 2013; Moradpour et al., 2014).

4.2 Aftershock productivity

We next focus on the variation of the number of triggered events or first generation of aftershocks N_{as} with the magnitude m of the trigger as displayed in Fig. 2. If averaged over triggers with the same m, we find an exponential scaling of the number of triggered

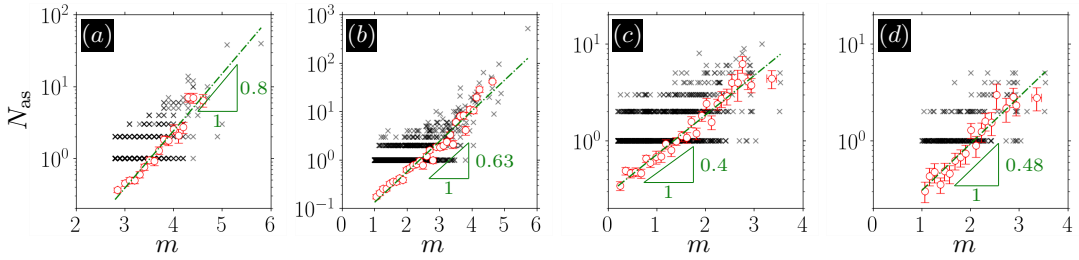

Figure 2. Number of aftershocks $N_{\rm as}(m)$ as a function of trigger magnitude m in **a)** Oklahoma and southern Kansas **b)** the Yuha Desert **c)** Long Valley Caldera with $b = 0.7, m_c = 0.2$ **d)** Long Valley Caldera with $b = 0.9, m_c = 1.0$. The symbols (-o-) indicate the mean value $\bar{N}_{\rm as}$ over prescribed bins. The error bars denote the standard error. The dash-dotted line indicates the productivity relation $\bar{N}_{\rm as} \propto 10^{\alpha m}$.

events with m in all cases, i.e., $N_{\rm as} \propto 10^{\alpha m}$ as also observed in tectonic settings (Dascher-Cousineau et al., 2020). The scaling exponent α controls the rate of exponential growth with m and we find that the value of α varies between catalogs. We obtain $\alpha \simeq 0.8$ for Oklahoma and southern Kansas, while in the Yuha Desert $\alpha \simeq 0.63$, and $\alpha < 0.5$ in the Long Valley Caldera. This implies that the productivity of triggers or mainshocks increases faster with magnitude in Oklahoma and southern Kansas than in the other cases while being comparable to tectonic systems (Gu et al., 2013; Moradpour et al., 2014). Note that variations in α have recently been attributed to mainshock properties and associated variations in terms of focal mechanisms, amplitude of stress drops, and on-fault slip distributions (Dascher-Cousineau et al., 2020), which might be at play for the different catalogs here as well. Note also that $\alpha \simeq 1.1$ has been reported in (T. Goebel et al., 2019) for Oklahoma and southern Kansas using a different methodology. The specific criteria to define and identify aftershocks might be responsible for the differences (Hainzl et al., 2013) since they are known to lead to significant biases in the estimation (Marsan & Helmstetter, 2017; Marsan & Lengline, 2008). In all cases, we find $\alpha < b$ implying that the overall event-event triggering budget is dominated by the more frequent smaller triggers instead of the fewer larger triggers (Gu et al., 2013).

4.3 Temporal aftershock rates

For a given event, the temporal rate of events it triggers varies with time. The insets of Fig. 3(a-d) display the daily aftershocks rates associated with triggers of magnitude m for our catalogs. In all cases, they follow approximately the OU relation $\lambda(t) = \frac{K}{(c+t)^p}$ over four to five decades, first established for tectonic earthquakes (Utsu et al., 1995; Davidsen & Baiesi, 2016). Here, t denotes the time after the trigger or mainshock, c is a characteristic timescale — whose origin is still debated (Davidsen & Baiesi, 2016; Hainzl, 2016) — separating the constant rate regime from an algebraically decaying one with exponent p, and K determines the maximum rate. For all case, we find $p \approx 1$, similar to what has been observed for tectonic earthquakes (Gu et al., 2013; Scholz, 2019). It is known that the used methodology has by construction a tendency to underestimate the true aftershock rates at late times (Davidsen & Baiesi, 2016) explaining the noticeably faster decay in the rates close to their respective maximum duration. Comparing the triggering rates for different trigger magnitudes, there is a general trend that the rates increase with m. Indeed, provided that c and p do not vary with m and m_c is fixed, the aftershock productivity relation discussed above implies that on average $K \propto 10^{\alpha m}$. This is directly tested in Fig. 3(a-d) by plotting $\lambda_m(t)/10^{\alpha m}$ against t. For all catalogs, we obtain a very good scaling collapse onto a master curve for almost all data. A noticeable exception is the rate for $m = 5.7$ in the Yuha Desert case, which corresponds to a *single* (and the largest) aftershock sequence and, thus, the deviation

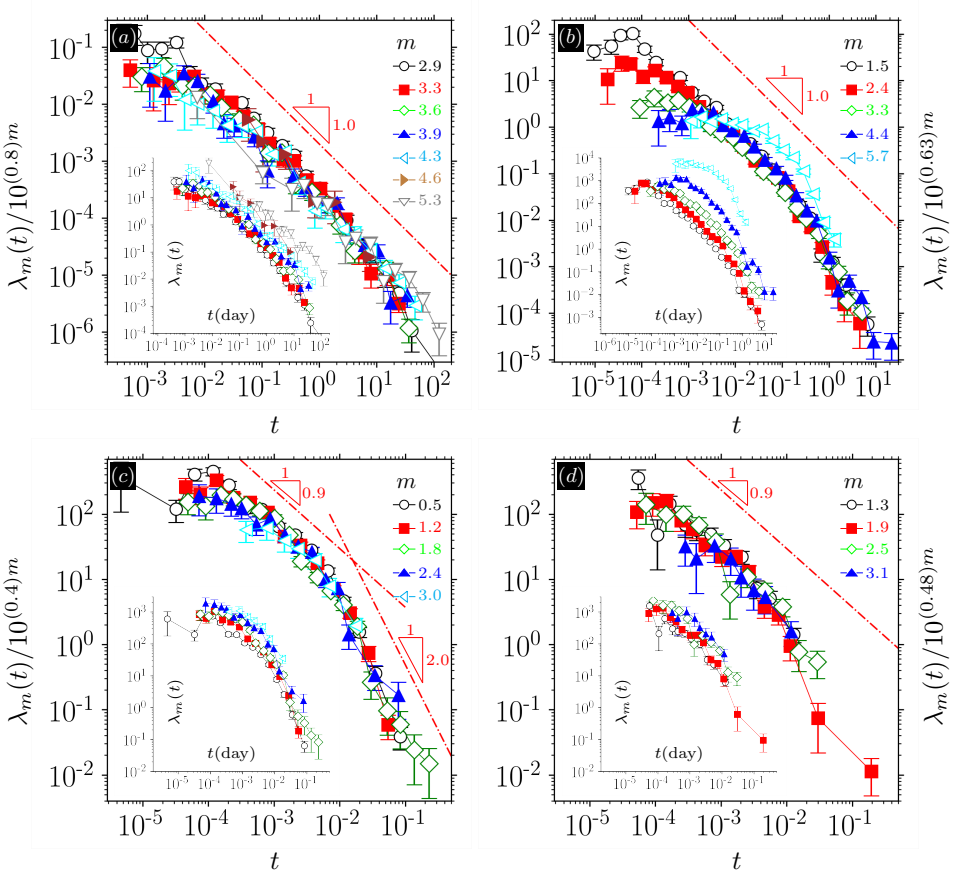

Figure 3. Rescaled aftershock rates $\lambda_m(t)/10^{\alpha m}$ versus time t in **a)** Oklahoma and southern Kansas **b)** the Yuha Desert, California **c)** Long Valley Caldera with $b = 0.7, m_c = 0.2$ **d)** Long Valley Caldera with $b = 0.9, m_c = 1.0$ for different mainshock magnitude ranges with mean magnitude m. Here, α denotes the productivity exponent as reported in Fig. 2. The (red) dash-dotted line indicates t^{-p}. The insets show the actual rates.

can likely be attributed to the natural variation in aftershock productivity discussed above. The scaling collapse on a master curve also shows that the Long Valley Caldera data in Fig. 3(c-d) may exhibit two different power-law regimes: an initial power-law with $p \simeq 1.0$ at $t < 10^{-2}$ (day) followed by a more rapid decay with exponent $\simeq 2$. Such a behavior is reminiscent of what has been observed in rock fracture (Davidsen et al., 2017; Baró & Davidsen, 2017). Fig. 3(a-d) also shows that only for the Yuha desert there are significant deviations from the master curve for smaller arguments indicating that c varies with the magnitude of the trigger, similar to what has been observed for tectonic earthquakes in southern California (Davidsen & Baiesi, 2016).

4.4 Triggering topology

Going beyond first generation of aftershocks, we focus on full triggering cascades or aftershock sequences. An aftershock sequence starts with a single (background) event that triggers its first generation of aftershocks, which in turn trigger the next generation of aftershocks and so on. This corresponds to the topology of a rooted tree (Zaliapin & Ben-Zion, 2013). In this representation, the "leaf depth", d_f, refers to the minimum number of generations between a given *leaf* (an event in the aftershock sequence that does not trigger an event) and the tree root. Averaging d_f over all leaves in a given tree provides insight into the

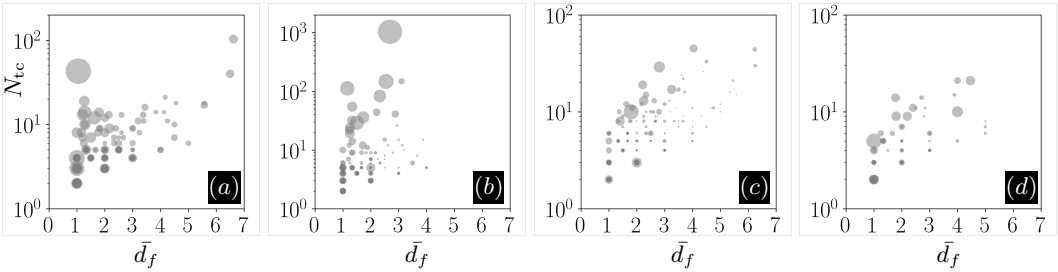

Figure 4. Number of events in the triggering cascade N_{tc} versus mean leaf depth $\bar{d}_f$ in **a)** Oklahoma and southern Kansas **b)** the Yuha Desert **c)** Long Valley Caldera with $b = 0.7, m_c = 0.2$ **d)** Long Valley Caldera with $b = 0.9, m_c = 1.0$. Symbol sizes represent magnitudes of the root events. The magnitude of the smallest and largest event are **a)** $2.8 - 5.8$ **b)** $1.0 - 5.7$ **c,d)** $0.2 - 3.5$. For the sake of clarity, a gray color scale is used indicating the relative density of overlapping data points.

shape of the triggering cascade. A large size (total number of events) of a triggering cascade N_{tc} associated with a small $\bar{d}_f$ indicates a burst-like topology, while small N_{tc} associated with a large $\bar{d}_f$ indicates a swarm-like topology. Figure 4(a-d) displays scatter plots of the relationship between $\bar{d}_f$ and N_{tc}. Comparing the different catalogs, we can identify both opposing behaviors. For the Long Valley Caldera in Fig. 4(c,d), the values of N_{tc} are comparatively small but $\bar{d}_f$ can take on relatively large values, while the Yuha Desert data show the opposite behavior. Thus, the natural swarm in the Long Valley Caldera tends to exhibit indeed a swarm-like topology, while the suspected swarms in the Yuha Desert tend to exhibit a more burst-like topology. Fig. 4(a) shows that the induced seismicity in Oklahoma and southern Kansas largely exhibits swarm-like behavior consistent with other findings for induced seismicity (Maghsoudi et al., 2018). However, the second largest aftershock sequence initiated by the largest event has almost exclusively first generation aftershocks representing a clear burst structure, consistent with the classical aftershock paradigm (Zaliapin & Ben-Zion, 2013). This triggering cascade and other exemplary ones are shown in Figs. S4-S6 in the SM.

5 Discussion

Our analysis of (suspected) fluid-induced seismicity in Oklahoma and southern Kansas, the Yuha Desert, and the Long Valley Caldera has shown the relevance of event-event triggering in all cases. Overall, this triggering obeys the GR relation, the aftershock productivity relation, the OU aftershock rate, and the scaling of the spatial aftershock zone with main shock magnitudes. Table 1 summarizes the relevant scaling relations and presents the estimated exponents based on our analysis and based on three independent studies, two of which probe aftershocks in natural swarms (Hainzl et al., 2013; Llenos & Michael, 2019) within the framework of the Epidemic-Type Aftershock-Sequence (ETAS) model, and the final one studies aftershocks in tectonic settings (Gu et al., 2013) using the same methodology we do.

There are a number of significant differences and commonalities in the scaling exponents that stand out. First, the aftershock productivity in Oklahoma and southern Kansas is high, $\alpha = 0.8$, and comparable to tectonic systems in southern California. All other catalogs have smaller values with the Long Valley Caldera having the lowest, $\alpha \approx 0.4$. Low α values were previously reported in a number of natural settings involving earthquake swarms, analogous to the Caldera region (Hainzl & Ogata, 2005). In addition, an ETAS-based study pertaining

Location (Year)	**Type**	**Gutenburg-Richter** $N \propto 10^{-b(m-m_c)}$ b	m_c	**Productivity** $N_{\text{as}} \propto 10^{\alpha m}$ α	**Omori-Utsu** $\lambda(t) \propto t^{-p}$ p	**Linear Density** $\rho(r) \propto r^{-\nu}$ ν	**Rupture Size** $r_{\text{rup}} \propto 10^{\sigma m}$ σ
Oklahoma & southern Kansas (2014−2017)	Fluid Induced (Man-made)	1.65	2.8	0.8	1.0	2.9	0.5
Long Valley Caldera, California (2014 *a*)	Natural Swarm	0.7	0.2	0.4	0.9	2.9	0.36
Long Valley Caldera, California (2014 *b*)	Natural Swarm	0.9	1.0	0.48	0.9	2.9	0.36
Yuha Desert, California (2010)	Fluid Induced (Natural)	0.95	1.0	0.6	1.0	1.7	0.4
Western Bohemia, Europe (2000 & 2008) (Hainzl et al., 2013)	Natural Swarm	0.9 & 1.25	0.5	0.61 − 0.68	1.33 − 1.37	–	–
San Ramon, California (1970−2015) (Llenos & Michael, 2019)	Natural Swarm	0.85	2.0	0.65	1.12	–	–
Southern California (1984−2005) (Gu et al., 2013)	Tectonic	1.09	2.5	0.85 − 0.9	1.2 − 1.25	1.6	0.4

Table 1. Comparison between estimated parameters and scaling exponents associated with different seismic catalogs and settings.

to swarm activities in Arkansas (Llenos & Michael, 2013) (which resembles the setting in Oklahoma) found that natural fluid flows lead to a lower aftershock productivity prior to injection-induced activity, as evidenced by smaller numerical estimates for α as well as for the constant of proportionality in the productivity relation. This is consistent with our observations and studies of induced seismicity related to hydraulic fracturing (Maghsoudi et al., 2018) suggesting that α allows one to distinguish between natural and human-made seismic swarms.

Second, the spatial density of aftershocks $\rho(r)$ falls off rapidly in Oklahoma and southern Kansas as well as in the Long Valley Caldera ($\nu = 2.9$), contrasted by long-range behavior in the Yuha Desert and also southern California with $\nu < 2$. In tectonic settings, the slow inverse power-law behavior of the aftershocks density $\rho(r) \propto r^{-\nu}$ beyond the rupture length can be explained by non-local transfer of static (Coulomb) stress within the brittle crust (Moradpour et al., 2014; Hainzl et al., 2014; van der Elst & Shaw, 2015). Given comparable estimates of ν between southern California (Gu et al., 2013) and the Yuha Desert, it is likely that the event-event triggering in the Yuha Desert is also largely driven by static stress changes. The relevance of such a triggering mechanism is consistent with the findings of our topology-based analysis, since the emerging *burstiness* may indicate the non-local transfer of internal stress within a rigid elastic medium (Zaliapin & Ben-Zion, 2013). On the other hand, our overall findings support that a rapid decay of the aftershock zone (with $\nu \approx 3$) is indicative of the dominant role of fluid migration. In particular, this mechanism might be relevant for induced events in Oklahoma and southern Kansas as well as for natural swarms in the Long Valley Caldera. Shelly et al. (2016) reported on the diffusive (and most likely localized) nature of the swarm propagation in the latter, which is another typical signature associated with various fluid-dominated contexts (Ruhl et al., 2016). In our study, swarm-like features were independently evidenced from the topology of triggering cascades in Caldera and (to a slightly lesser extent) Oklahoma.

Narrow aftershock zones for Oklahoma and southern Kansas were independently reported in (Rosson et al., 2019) based on a spatio-temporal windowing approach. Rosson et al. (2019) argued that the absence of long-range triggering might also be due to structural

heterogeneities within the fault network in Oklahoma and southern Kansas, which could substantially constrain inter-fault activation in the region (Alt & Zoback, 2016). Similar arguments were made in (Shelly et al., 2016) pointing to the complex fault geometry in Caldera, which potentially led to confined swarm activities in this natural setting. Altogether, the complex interplay between fluid migration and local heterogeneities appear to control the spatial extent of aftershock triggering in Oklahoma as well as Caldera.

As for the Omori exponent, Table 1 shows that $p \approx 1$ appears to be a robust measurement although there is a slightly faster decay associated with natural swarms in Bohemia (Hainzl et al., 2013) and perhaps tectonic-based earthquakes in southern California, which is expected for strike-slip faulting (Tahir & Grasso, 2015). Despite being distinguishable in terms of spatial aftershocks densities and productivity, both Oklahoma and the Yuha Desert exhibit statistically similar temporal features. This is in line with recent observations made by (Rosson et al., 2019) comparing the induced setting in Oklahoma with the tectonics-based seismicity in southern California. We note that the latter is known to have well-established seismic features (Gu et al., 2013), which are comparatively close to what we find for the Yuha Desert (Table 1). We observed analogous temporal properties between the Caldera and Oklahoma case studies that, along with spatial similarities, might be indicative of the swarm-type evolution in fluid-induced settings.

6 Conclusions

We have identified common features of event-event triggering between human-made and natural seismicity in fluid-driven contexts. Two natural case studies, Long Valley Caldera and the Yuha Desert, were used as benchmarks, in which the fluid migration was (partially) involved. We recovered essential features of natural swarm-like activities in injection-induced seismicity in Oklahoma and southern Kansas. Most remarkably, the "swarminess" manifested itself in narrow spatial aftershock zones and associated triggering topology that did not match tectonic mainshock-aftershock sequences in addition to the absence of Båth's law. Finally, high aftershock productivity associated with human-made swarms appears to be a robust indicator making them distinguishable from naturally-induced swarms, which is of direct importance for earthquake forecasting and seismic hazard analysis.

Acknowledgments

Sponsors of the Microseismic Industry Consortium are sincerely thanked for their support of this initiative. This work was supported by funding from a Collaborative Research and Development grant from the Natural Sciences and Engineering Research Council of Canada.

Data Availability Statement

Datasets for this research are included in (Schoenball & Ellsworth, 2017a), (Ross et al., 2017), and (Shelly et al., 2016).

References

Alt, R. C., & Zoback, M. D. (2016). In situ stress and active faulting in Oklahoma. *Bulletin of the Seismological Society of America*, *107*(1), 216–228.

Baró, J., & Davidsen, J. (2017). Are triggering rates of labquakes universal? inferring triggering rates from incomplete information. *The European Physical Journal Special Topics*, *226*(15), 3211–3225.

Bhattacharya, P., Phan, M., & Shcherbakov, R. (2011). Statistical analysis of the 2002 Mw 7.9 Denali earthquake aftershock sequence. *Bulletin of the Seismological Society of America*, *101*(6), 2662–2674.

Brengman, C. M., Barnhart, W. D., Mankin, E. H., & Miller, C. N. (2019). Earthquake-

scaling relationships from geodetically derived slip distributions. *Bulletin of the Seismological Society of America*, *109*(5), 1701–1715.

Dascher-Cousineau, K., Brodsky, E. E., Lay, T., & Goebel, T. H. (2020). What controls variations in aftershock productivity? *Journal of Geophysical Research: Solid Earth*.

Davidsen, J., & Baiesi, M. (2016). Self-similar aftershock rates. *Physical Review E*, *94*(2), 022314.

Davidsen, J., Gu, C., & Baiesi, M. (2015). Generalized Omori–Utsu law for aftershock sequences in southern California. *Geophysical Journal International*, *201*(2), 965–978.

Davidsen, J., Kwiatek, G., Charalampidou, E.-M., Goebel, T., Stanchits, S., Rück, M., & Dresen, G. (2017). Triggering processes in rock fracture. *Physical Review Letters*, *119*(6), 068501.

Deflandre, J.-P. (2016). Induced microseismicity: Short overview, state of the art and feedback on source rock production. *The Open Petroleum Engineering Journal*, *9*(1).

Dinske, C., & Shapiro, S. A. (2013). Seismotectonic state of reservoirs inferred from magnitude distributions of fluid-induced seismicity. *Journal of seismology*, *17*(1), 13–25.

Eaton, D. W., Davidsen, J., Pedersen, P. K., & Boroumand, N. (2014). Breakdown of the Gutenberg-Richter relation for microearthquakes induced by hydraulic fracturing: influence of stratabound fractures. *Geophysical Prospecting*, *62*(Vertical Seismic Profiling and Microseismicity Frontiers), 806–818.

Eaton, D. W., & Maghsoudi, S. (2015). 2b... or not 2b? interpreting magnitude distributions from microseismic catalogs. *First Break*, *33*(10), 79–86.

Ellsworth, W. L. (2013). Injection-induced earthquakes. *Science*, *341*(6142), 1225942.

Eyre, T. S., Eaton, D. W., Garagash, D. I., Zecevic, M., Venieri, M., Weir, R., & Lawton, D. C. (2019). The role of aseismic slip in hydraulic fracturing–induced seismicity. *Science advances*, *5*(8), eaav7172.

Gneiting, T., Ševčíková, H., & Percival, D. B. (2012). Estimators of fractal dimension: Assessing the roughness of time series and spatial data. *Statistical Science*, 247–277.

Goebel, T., Rosson, Z., Brodsky, E., & Walter, J. (2019). Aftershock deficiency of induced earthquake sequences during rapid mitigation efforts in Oklahoma. *Earth and Planetary Science Letters*, *522*, 135–143.

Goebel, T. H., & Brodsky, E. E. (2018). The spatial footprint of injection wells in a global compilation of induced earthquake sequences. *Science*, *361*(6405), 899–904.

Gu, C., Schumann, A. Y., Baiesi, M., & Davidsen, J. (2013). Triggering cascades and statistical properties of aftershocks. *Journal of Geophysical Research: Solid Earth*, *118*(8), 4278–4295.

Hainzl, S. (2016). Rate-dependent incompleteness of earthquake catalogs. *Seismological Research Letters*, *87*(2A), 337–344.

Hainzl, S., Moradpour, J., & Davidsen, J. (2014). Static stress triggering explains the empirical aftershock distance decay. *Geophysical Research Letters*, *41*(24), 8818–8824.

Hainzl, S., & Ogata, Y. (2005). Detecting fluid signals in seismicity data through statistical earthquake modeling. *Journal of Geophysical Research: Solid Earth*, *110*(B5).

Hainzl, S., Zakharova, O., & Marsan, D. (2013). Impact of aseismic transients on the estimation of aftershock productivity parameters. *Bulletin of the Seismological Society of America*, *103*(3), 1723–1732.

Kagan, Y. Y. (2013). *Earthquakes: models, statistics, testable forecasts*. John Wiley & Sons.

Kantz, H., & Schreiber, T. (2004). *Nonlinear time series analysis* (Vol. 7). Cambridge university press.

Langenbruch, C., & Zoback, M. D. (2016). How will induced seismicity in Oklahoma respond to decreased saltwater injection rates? *Science advances*, *2*(11), e1601542.

Leonard, M. (2010). Earthquake fault scaling: Self-consistent relating of rupture length, width, average displacement, and moment release. *Bulletin of the Seismological Society of America*, *100*(5A), 1971–1988.

Llenos, A. L., & Michael, A. J. (2013). Modeling earthquake rate changes in Oklahoma and Arkansas: Possible signatures of induced seismicity. *Bulletin of the Seismological Society of America*, *103*(5), 2850–2861.

Llenos, A. L., & Michael, A. J. (2019). Ensembles of etas models provide optimal operational earthquake forecasting during swarms: Insights from the 2015 San Ramon, California swarm. *Bulletin of the Seismological Society of America*, *109*(6), 2145–2158.

Maghsoudi, S., Baró, J., Kent, A., Eaton, D., & Davidsen, J. (2018). Interevent triggering in microseismicity induced by hydraulic fracturing. *Bulletin of the Seismological Society of America*, *108*(3A), 1133–1146.

Maghsoudi, S., Eaton, D. W., & Davidsen, J. (2016). Nontrivial clustering of microseismicity induced by hydraulic fracturing. *Geophysical Research Letters*, *43*(20), 10–672.

Marsan, D., & Helmstetter, A. (2017). How variable is the number of triggered aftershocks? *Journal of Geophysical Research: Solid Earth*, *122*(7), 5544–5560.

Marsan, D., & Lengline, O. (2008). Extending earthquakes' reach through cascading. *Science*, *319*(5866), 1076–1079.

Moradpour, J., Hainzl, S., & Davidsen, J. (2014). Nontrivial decay of aftershock density with distance in southern California. *Journal of Geophysical Research: Solid Earth*, *119*(7), 5518–5535.

Ross, Z. E., Rollins, C., Cochran, E. S., Hauksson, E., Avouac, J.-P., & Ben-Zion, Y. (2017). Aftershocks driven by afterslip and fluid pressure sweeping through a fault-fracture mesh. *Geophysical Research Letters*, *44*(16), 8260–8267.

Rosson, Z., Walter, J., Goebel, T., & Chen, X. (2019). Narrow spatial aftershock zones for induced earthquake sequences in Oklahoma. *Geophysical Research Letters*, *46*(17-18), 10358–10366.

Ruhl, C., Abercrombie, R., Smith, K., & Zaliapin, I. (2016). Complex spatiotemporal evolution of the 2008 Mw 4.9 Mogul earthquake swarm (Reno, Nevada): Interplay of fluid and faulting. *Journal of Geophysical Research: Solid Earth*, *121*(11), 8196–8216.

Schoenball, M., Davatzes, N. C., & Glen, J. M. (2015). Differentiating induced and natural seismicity using space-time-magnitude statistics applied to the Coso geothermal field. *Geophysical Research Letters*, *42*(15), 6221–6228.

Schoenball, M., & Ellsworth, W. L. (2017a). A systematic assessment of the spatiotemporal evolution of fault activation through induced seismicity in Oklahoma and southern Kansas. *Journal of Geophysical Research: Solid Earth*, *122*(12).

Schoenball, M., & Ellsworth, W. L. (2017b). Waveform-relocated earthquake catalog for Oklahoma and southern kansas illuminates the regional fault network. *Seismological Research Letters*, *88*(5), 1252–1258.

Scholz, C. H. (2019). *The mechanics of earthquakes and faulting*. Cambridge university press.

Shapiro, S. A. (2015). *Fluid-induced seismicity*. Cambridge University Press.

Shelly, D. R., Ellsworth, W. L., & Hill, D. P. (2016). Fluid-faulting evolution in high definition: Connecting fault structure and frequency-magnitude variations during the 2014 Long Valley Caldera, California, earthquake swarm. *Journal of Geophysical Research: Solid Earth*, *121*(3), 1776–1795.

Skoumal, R. J., Brudzinski, M. R., & Currie, B. S. (2015). Distinguishing induced seismicity from natural seismicity in Ohio: Demonstrating the utility of waveform template matching. *Journal of Geophysical Research: Solid Earth*, *120*(9), 6284–6296.

Tahir, M., & Grasso, J. R. (2015). Faulting style controls for the space–time aftershock patterns. *Bulletin of the Seismological Society of America*, *105*(5), 2480–2497.

Teng, G., & Baker, J. W. (2019). Seismicity declustering and hazard analysis of the Oklahoma–Kansas region. *Bulletin of the Seismological Society of America*, *109*(6), 2356–2366.

Utsu, T., Ogata, Y., et al. (1995). The centenary of the Omori formula for a decay law of aftershock activity. *Journal of Physics of the Earth*, *43*(1), 1–33.

van der Elst, N. J., & Shaw, B. E. (2015). Larger aftershocks happen farther away: Nonseparability of magnitude and spatial distributions of aftershocks. *Geophysical Research*

Letters, *42*(14), 5771–5778.

Vasylkivska, V. S., & Huerta, N. J. (2017). Spatiotemporal distribution of Oklahoma earthquakes: Exploring relationships using a nearest-neighbor approach. *Journal of Geophysical Research: Solid Earth*, *122*(7), 5395–5416.

Zaliapin, I., & Ben-Zion, Y. (2013). Earthquake clusters in southern California ii: Classification and relation to physical properties of the crust. *Journal of Geophysical Research: Solid Earth*, *118*(6), 2865–2877.

Zaliapin, I., Gabrielov, A., Keilis-Borok, V., & Wong, H. (2008). Clustering analysis of seismicity and aftershock identification. *Physical Review Letters*, *101*(1), 018501.